Structural origins of electronic conduction in amorphous copper-doped alumina

K. N. Subedi,[1,*] K. Prasai,[2] M. N. Kozicki,[3] and D. A. Drabold[1,†]
[1]*Department of Physics and Astronomy, Ohio University, Athens, Ohio 45701, USA*
[2]*E. L. Ginzton Lab, Stanford University, Stanford, California 94305, USA*
[3]*School of Electrical, Computer and Energy Engineering, Arizona State University, Tempe, Arizona 85287, USA*

(Received 18 February 2019; published 28 June 2019)

We perform an *ab initio* modeling of amorphous copper-doped alumina (a-Al_2O_3:Cu), a prospective memory material based on resistance switching, and study the structural origin of electronic conduction in this material. We generate molecular dynamics based models of a-Al_2O_3:Cu at various Cu concentrations and study the structural, electronic, and vibrational properties as a function of Cu concentration. Cu atoms show a strong tendency to cluster in the alumina host, and metallize the system by filling the band gap uniformly for higher Cu concentrations. We also study thermal fluctuations of the HOMO-LUMO energy splitting and observe the time evolution of the size of the band gap, which can be expected to have an important impact on the conductivity. We perform a numerical computation of conduction pathways, and show its explicit dependence on Cu connectivity in the host. We present an analysis of ion dynamics and structural aspects of localization of classical normal modes in our models.

DOI: 10.1103/PhysRevMaterials.3.065605

I. INTRODUCTION

Nonvolatile memory devices based on resistive switching characteristics have been studied since the late 1960′s [1]. In these devices, application of an external bias potential across an electrolyte changes the electrical conductivity of the electrolyte by changing its structure. This process is reversible and can be performed in the timescale of nanoseconds. Three types of resistive random access memory (RRAM) devices have been studied in detail [2] and these include RRAM based on oxygen vacancies, RRAM based on thermochemical effects, and RRAM based on the electrochemical metallization. The latter class of devices are also called conducting bridge random access memory or CBRAM. The CBRAM devices are composed of a thin solid electrolyte layer placed between an oxidizable anode (e.g., Cu, Ag, or TiN) and an inert cathode (e.g., W or Pt). The Cu, in its ionic state, is converted into the conducting "filament" by the applied field: the ions are reduced by electrons flowing from the cathode to leave them in their metallic form, although other counterions (e.g., OH-) may also be involved in this process [3]. With the application of a reverse bias, the connectivity of the cluster can be destroyed, and the device is put into a highly electronically resistive state. The details of the mechanism of CBRAMs have been described elsewhere [4,5]. The performance of CBRAM devices has been studied with several materials as the solid electrolyte which include chalcogenides [6,7], insulating metal oxides [8–14], and bilayer materials [15,16]. CBRAM devices have demonstrated excellent performance in terms of operational voltage, read/write speed, endurance, and data retention. Among the host materials reviewed for CBRAM devices, alumina (Al_2O_3) shows particular promise. It has a high dielectric constant, large band gap, and its amorphous phase is highly stable [17,18]. The experimental results for CBRAM devices based on Cu alloyed with Al_2O_3 have shown that the cell exhibits highly controlled set and reset operations, fast pulse programming (10 ns) at low voltage ($<$3 V), and low-current (10 μA) with 10^6 cycles per second for the writing speed [12].

In our recent work [19], we developed a method to compute a space-projected conductivity (SPC) and utilized the method to visualize the conduction-active parts of the network for two different CBRAM materials, metal-doped a-Al_2O_3 and a-$GeSe_3$. We observed that the Cu atoms cluster and the clustered Cu atoms form a conducting pathways in a-Al_2O_3 whereas the Ag atoms are more or less uniformly distributed in the a-$GeSe_3$.

In this paper, we further investigate the microscopic origin of electronic conduction in Cu-doped a-Al_2O_3. We use *ab initio* molecular dynamics (AIMD) to generate atomic models of a-Al_2O_3:Cu for varying Cu concentrations. The work presented in this paper shows that an increase in local Cu concentration can result in stable conducting pathways due to the strong tendency of Cu atoms to cluster in the ionic host. This would lead to a highly stable low-resistance state (LRS) for high copper concentration, which does indeed seem to be the case for copper-alumina devices [12]. We study the electronic properties for these models and are able to crudely estimate the local concentration of Cu above which CBRAM device switches to the LRS. We present the numerical computation of conduction-active parts of the network by computing SPC, and show that the strong electron-lattice coupling for electron states near the gap leads to interesting and substantial thermally induced conductivity fluctuations on a picosecond timescale. We study the lattice dynamics for the doped models and show that the lower frequency vibrational modes correspond to the Cu atoms.

*ks173214@ohio.edu
†drabold@ohio.edu

TABLE I. Initial and final densities of a-Al_2O_3:Cu models.

Cu content	Mol. formula	ρ_{in} (g/cc)	ρ_f (g/cc)
0%	$(Al_2O_3)_{1.00}Cu_{0.00}$	3.175	3.175
10%	$(Al_2O_3)_{0.90}Cu_{0.10}$	3.58	3.75
20%	$(Al_2O_3)_{0.80}Cu_{0.20}$	3.78	3.99
30%	$(Al_2O_3)_{0.70}Cu_{0.30}$	4.53	4.82

The rest of the paper is organized as follows. Section II describes computational details used to create the structures and also the details of our method to obtain the SPC. Section III includes results where we discuss structural, electronic, and dynamical properties of the models in different subsections. Section IV provides the conclusions.

II. COMPUTATIONS

A. Model generation

In this work, we use AIMD to generate four atomic models with the composition of $(a\text{-}Al_2O_3)_{1-n}Cu_n$ with $n = 0$, 0.1, 0.2, and 0.3. We used a density of 3.175 g/cm^3 for a-Al_2O_3 [20,21]. For the Cu-doped models, we referred to the literature [22] to make an initial guess, then carried out a zero-pressure relaxation to correct/optimize the result. For each model, we began by taking a cubic supercell of 200 atoms with randomly initialized atomic positions. Plane-wave density functional calculations were performed using the VASP package [23] and projector-augmented wave (PAW) [24,25] potentials within the local density approximation (LDA) [26] using periodic boundary conditions. We used a kinetic energy cutoff of 420 eV and the Γ point to sample the Brillouin zone. A time step of 1.5 fs was used and the temperature was controlled by a Nosé-Hoover thermostat throughout.

We performed a melt-quench simulation [27] with a starting temperature of 3500 K. After annealing the "hot liquid" for 7.5 ps at 3500 K, we cooled each model to 2600 K at a rate of 0.27 K/fs as discussed in [28] and then equilibrated for 10 ps. Each model was then quenched to 300 K at the same cooling rate 0.27 K/fs and further equilibrated for another 10 ps. Zero-pressure relaxations were used to determine the final densities for Cu-doped models. The final force on each atom is no more than 0.01 eV/Å. The initial and final densities are provided in Table I.

B. Spatial projection of electronic conductivity

In this section, we briefly discuss a method to obtain a space-projected electronic conductivity. We discuss the method in detail in Ref. [19]. We begin by writing the diagonal elements of the conductivity tensor for each k point $\mathbf{k}$ and frequency ω using the standard Kubo-Greenwood formula (KGF) [29,30] as

$$\sigma_{\mathbf{k}}(\omega) = \frac{2\pi e^2}{3m^2\omega\Omega}\sum_{i,j}\sum_{\alpha}[f(\epsilon_{i,\mathbf{k}}) - f(\epsilon_{j,\mathbf{k}})] \times |\langle\psi_{j,\mathbf{k}}|p^{\alpha}|\psi_{i,\mathbf{k}}\rangle|^2\delta(\epsilon_{j,\mathbf{k}} - \epsilon_{i,\mathbf{k}} - \hbar\omega). \quad (1)$$

In the above equation (1), e and m represent the charge and mass of the electron, respectively. Ω represents the volume of the supercell. We average over diagonal elements of conductivity tensor ($\alpha = x, y, z$). $\psi_{i,\mathbf{k}}$ is the Kohn-Sham orbital associated with energy $\epsilon_{i,\mathbf{k}}$ and $f(\epsilon_{i,\mathbf{k}})$ denotes the Fermi-Dirac weight. p^{α} is the momentum operator along each Cartesian direction α. Let

$$g_{ij}(\mathbf{k},\omega) = \frac{2\pi e^2}{3m^2\omega\Omega}[f(\epsilon_{i,\mathbf{k}}) - f(\epsilon_{j,\mathbf{k}})]\delta(\epsilon_{j,\mathbf{k}} - \epsilon_{i,\mathbf{k}} - \hbar\omega).$$

Then, suppressing the explicit dependence of σ on $\mathbf{k}$ and ω, the conductivity can be expressed as

$$\sigma = \sum_{i,j,\alpha} g_{ij}\int d^3x\int d^3x'[\psi_j^*(x)p^{\alpha}\psi_i(x)][\psi_i^*(x')p^{\alpha}\psi_j(x')], \quad (2)$$

a form that reminds of the the current-current correlation function origins of Kubo's approach. If we define complex-valued functions $\xi_{ij}^{\alpha}(x) = \psi_i^*(x)p^{\alpha}\psi_j(x)$ on a real-space grid (call the grid points $\mathbf{x}$) with uniform spacing of width h in three dimensions, then we can approximate the integrals as a sum on the grid. Thus, Eq. (2) can be written as

$$\sigma \approx h^6\sum_{x,x'}\sum_{i,j,\alpha} g_{ij}\xi_{ji}^{\alpha}(x)\xi_{ij}^{\alpha}(x'). \quad (3)$$

In the preceding, the approximation becomes exact as $h \to 0$. If we define a Hermitian, positive-semidefinite matrix

$$\Gamma(x,x') = \sum_{i,j,\alpha} g_{ij}\xi_{ji}^{\alpha}(x)\left(\xi_{ji}^{\alpha}(x')\right)^*, \quad (4)$$

we can spatially decompose the conductivity at each grid point as $\zeta(x) = |\sum_{x'}\Gamma(x,x')|$. $\zeta(x)$ contains vital information about the conduction-active parts of the system.[1] The form of ζ makes use of a common approximation for conductivity estimates in disordered systems, namely, averaging over the diagonal elements of the conduction tensor. Thus images of $\zeta(x)$ made in this way should be thought of as indicating those parts of the network that would support a current through the system with ideal leads in the x, y, and z directions.

To implement the method, we used VASP and associated Kohn-Sham orbitals $\psi_{i,\mathbf{k}}$. We divided the supercell into $36\times 36\times 36$ (dim$\Gamma = 46\,656$) grid points and obtained the wave function at each point by using the convenient code of Feenstra and Widom [31]. In computing the ξ_{ij}^{α}, we used a centered finite-difference method to compute the gradient of ψ_i for each α. We used an electronic temperature of $T = 1000$ K for the Fermi-Dirac distribution. We approximated the δ function in Eq. (1) by a Gaussian distribution of width kT, where k is Boltzmann's constant. In this paper we restrict ourselves to the case of $\omega = 0$. We note that the value of the conductivity from an expression such as Eq. (3) is somewhat dependent upon the

[1] A simpler scheme is to just look at the structure of the Kohn-Sham eigenfunctions near the Fermi level to identify the conduction active parts of the network. While this is a sensible first approximation, it entirely neglects the current-current correlations that underlie the derivation of the Kubo formula from linear response theory.

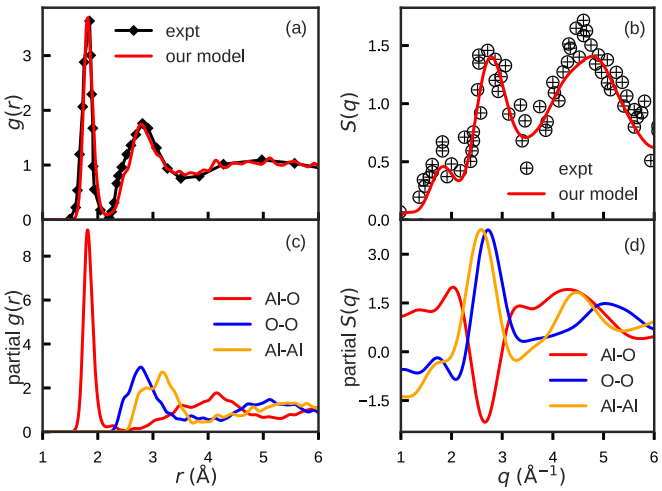

FIG. 1. $g(r)$ and $S(q)$ of a-Al_2O_3: (a) $g(r)$ computed on models are compared with measured $g(r)$. (b) $S(q)$ computed on models are compared with measured $S(q)$. (c), (d) Partial $g(r)$ and partial $S(q)$, respectively, for Al-O, O-O, and Al-Al pairs.

smearing of the δ function (temperature T), but the structure of the SPC ζ is far less so.

The first appearance (to our knowledge) of an equation of the form shown in Eq. (2) (obtained from the Kubo-Greenwood formula in one dimension) was in a paper of Economou and Soukoulis [32]. Baranger and Stone [33] elegantly generalized this with the inclusion of a magnetic field, and worked out the current density within linear response. These formulas were applied to a two-dimensional (2D) Anderson model, yielding interesting results even for a relatively simple system [34]. Our work is different from the preceding in at least two senses: first, we adapt this general approach to practical materials problems using fairly realistic (Kohn-Sham) wave functions. Also, though we do not exploit it here, the eigenvalues and eigenvectors of the positive-semidefinite matrix Γ are interesting objects. Invariably, only a tiny fraction of these eigenvalues are significantly different from zero, and the remaining handful of eigenvectors conjugate to nonzero eigenvalues specify the key conduction "modes" of the system [35].

III. RESULTS

A. Structural and electronic properties

1. Bonding and topology of the models

As a test of validity of our models, we compute the total radial distribution function $g(r)$ on a-Al_2O_3 models and compare with experimentally measured neutron scattering $g(r)$ from [36]. A plot showing these two $g(r)$ is presented in Fig. 1 and shows that the models capture the structural order up to 6 Å reasonably well. We also compute the structure factor $S(q)$ on our models at 2600 K and compare it with $S(q)$ measured on l-Al_2O_3 [37]. The plot shows that these two $S(q)$ show a satisfactory agreement, especially on the positions of peaks at 1.8, 2.8, and 4.7 Å^{-1}. The bottom left plot in Fig. 1 presents the partial $g(r)$ computed on models of a-Al_2O_3. The peaks at 1.81, 2.78, and 3.17 Å correspond to the geometrical bond distances for Al-O, O-O, and Al-Al pairs, respectively; these results are in agreement with similar earlier works [38–40]. The bottom right plot in Fig. 1 shows the partial $S(q)$ corresponding to Al-Al, Al-O, and O-O pairs computed on a-Al_2O_3 models. We see that the first peak in the total $S(q)$ occurs at 2.8 Å^{-1} due to the partial cancellation arising from Al-O correlations.

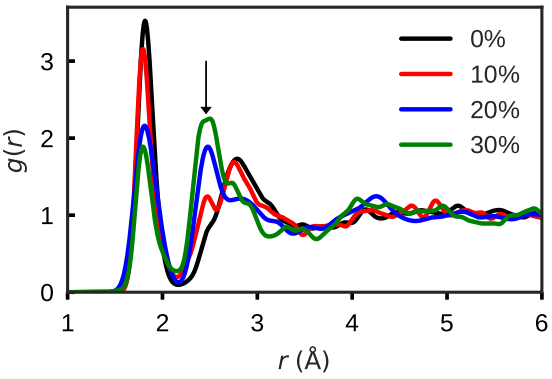

FIG. 2. Total $g(r)$ computed from the models of a-Al_2O_3:Cu at various concentrations of Cu. The hump appearing in Cu-doped models, indicated by arrow, originates from Cu-Cu correlation.

For doped models, the computed $g(r)$ are plotted in Fig. 2 and show that the position of first peak remains largely the same as undoped a-Al_2O_3 suggesting that Al-O bond remains unaltered. As the concentration of Cu increases, a hump corresponding to Cu-Cu correlation appears and grows at $r \approx$ 2.44 Å. The relative sharpness of Cu-Cu hump, even for the lowest concentration of Cu, provides a hint that Cu atoms are probably clustered. Indeed, a visual inspection of the models, shown here in Fig. 3, clearly shows the strong tendency of Cu atoms to cluster.

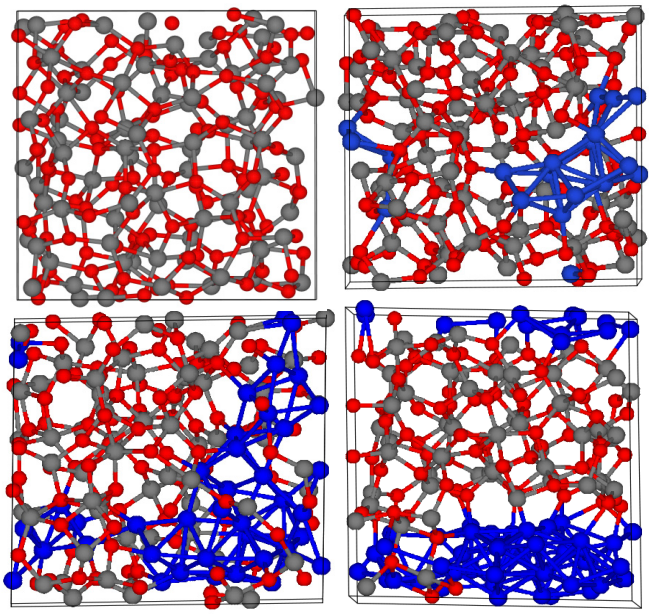

FIG. 3. Final relaxed a-Al_2O_3:Cu models. Top plots (from left) represent for 0% and 10% Cu and bottom plots (from left) represent for 20% and 30% Cu. Atom's color: Al (gray), Cu (blue), and O (red).

TABLE II. Average coordination numbers around Cu atoms for 10%, 20%, and 30% Cu models.

Cu content(%)	Cu-O	Cu-Cu	Cu-Al
10	1.15	5.1	3.0
20	0.68	6.85	2.45
30	0.48	8.27	1.78

It is significant that Cu strongly tends to cluster. A study by Dawson and Robertson [41] asserts that the Cu-Cu interactions become more favorable with increasing Cu content. We study the average coordination number around Cu atom at different Cu concentrations as shown in Table II. We take the first minimum in suitable partial $g(r)$ as the cutoff distance to define the coordination number. The increase in Cu coordination by Cu and the decrease in Cu coordination by Al and O implies the segregation of Cu from the host and formation of cluster.

2. *Electronic structure*

a. Density of states and the localization. Alloying with copper in a-Al_2O_3 is expected to have effects on electronic properties which are of interest for applications of these materials in CBRAM devices. We investigate these effects by examining the density of Kohn-Sham eigenvalues (EDOS) and their spatial localization. The localization is gauged by computing the inverse participation ratio (IPR) that is defined as IPR $= \sum_i {a_{ni}}^4/(\sum_i {a_{ni}}^2)^2$ [42], where the a'_{ni}s are the contribution to eigenfunction ψ_n from the ith atomic projected orbital obtained from VASP. The values of IPR extend from nearly 0 to 1. The states with higher IPR values are more localized. Figure 4 shows the computed EDOS and IPR as a function of Cu concentration. We find a decrease in HOMO-LUMO gap with increasing Cu concentration; at Cu concentration 20% and 30%, the EDOS is continuous across the Fermi level. The states that fill in the band gap are quite extended as indicated by small values of IPR around the Fermi level in Fig. 4. The mean IPR values around the gap declines monotonically with Cu concentration.

To physically interpret the connection of the HOMO-LUMO gap and the extent of localization with electronic conductivity (σ), let us rewrite Eq. (1) for the dc conductivity ($T = 0$ K) in the form of Mott and Davis [43]:

$$\sigma_{\rm dc} = \frac{2\pi e^2 \hbar \Omega}{m^2} |D_{\epsilon_f}|^2 N^2(\epsilon_f), \tag{5}$$

where D_{ϵ_f} is a matrix element of ∇_α between Kohn-Sham states near the Fermi level and $N(\epsilon_f)$ is the density of states. For small gap, one expects more states near the Fermi level. The magnitude of matrix elements D_{ϵ_f} for extended states would be higher. So, the conductivity could be crudely linked with the HOMO-LUMO gap of the material and the extent of localization of the Kohn-Sham states.

By projecting the electronic states onto atomic sites, we observe that the states near the Fermi level for the doped models consist of Cu orbitals. An example of the site-projected EDOS, for 20% Cu, is plotted in Fig. 5. It is quite interesting that at 20% and 30% Cu concentrations, Cu levels almost

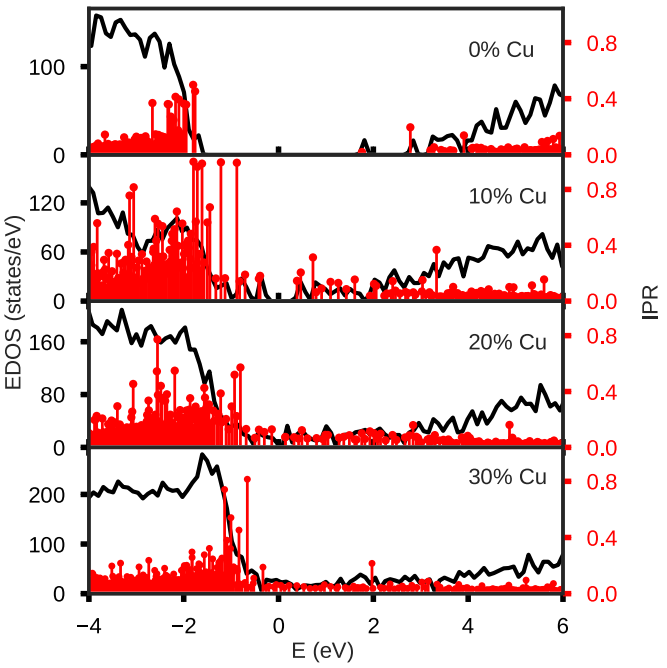

FIG. 4. Electronic density of states (EDOS) and the inverse participation ratio (IPR) computed from a-Al_2O_3:Cu models for different concentrations of Cu. The black curve represents EDOS and red vertical lines show IPR. The Fermi level is shifted to zero in all plots.

uniformly fill the host a-Al_2O_3 gap as shown in Fig. 4. The Cu does not form an impurity band, as one might naively suppose from experience on heavily doped semiconductors. In Fig. 4, we see that the models with higher Cu concentration produce states near Fermi level that yield an essentially metallic form of conduction. This is qualitatively different than the case of Ag in $GeSe_3$ [44], wherein the Ag atoms do not cluster

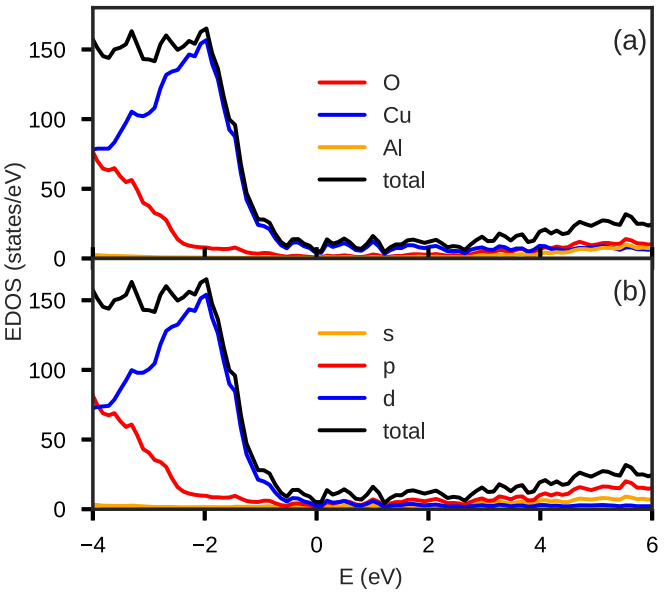

FIG. 5. Projected electronic density of states (EDOS) computed from a-Al_2O_3:Cu models with 20% Cu. (a) Site-projected EDOS. (b) Orbital-projected EDOS. The Fermi energy is shifted to zero.

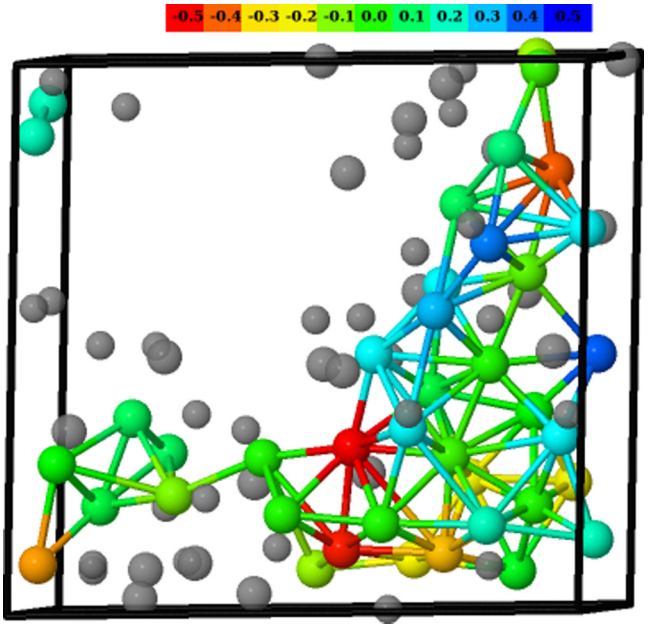

FIG. 6. Net Bader charge on Cu atoms calculated from a-Al_2O_3:Cu models with 20% Cu concentration. A color code displayed on top is used to represent the charge state. Charge state of zero, shown by green, represents a neutral Cu atom; the charge values are in units of electronic charge. All Cu atoms are shown in color. Light gray atoms represent Al and O atoms within the first cutoff distance of Cu atoms.

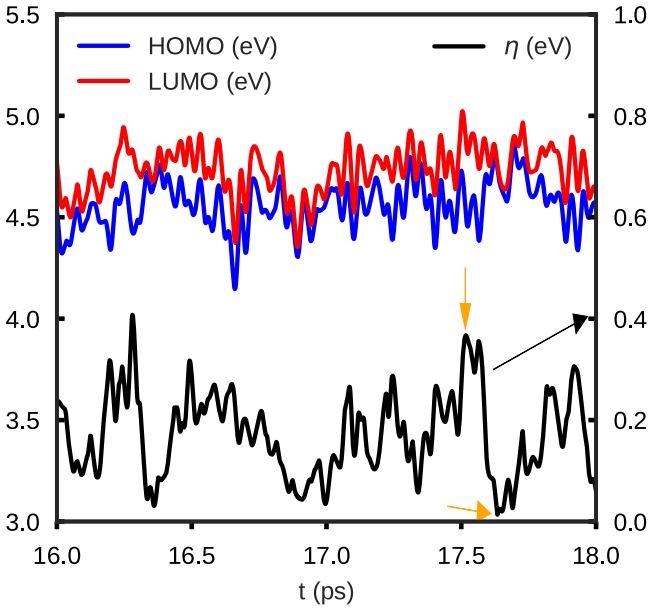

FIG. 7. Fluctuation of HOMO, LUMO, and HOMO-LUMO gap (η) with time for 20% model at 1000 K. $\eta(t)$ is represented by black line with its values given by right axis of the plot as shown by arrowhead in the plot.

and do not introduce states in the optical gap of the host. A comprehensive study on chalcogenides [45] shows that states near the Fermi level are mainly contributed from chalcogen atoms for lower concentration of Cu (<25%) and for higher concentrations, Cu-derived states appear along with the chalcogen states. So, Cu in chalcogenides behave differently compared to Cu in alumina. We observe that electron states in the alumina gap are filled mostly by $3d$, $4s$, and $4p$ orbitals of Cu.

b. Charge analysis on Cu atoms. The formation of Cu clusters in a-Al_2O_3 matrix leaves the Cu atoms in different charge states depending on the local environment of these Cu atoms with O and/or Al atoms. We performed Bader charge analysis [46] to calculate net charge on these atoms and an analysis for 20% Cu-doped model is shown in Fig. 6. The charge state of the Cu atoms (shown in color in Fig. 6) can be explained by a simple analysis of the first neighbors around the Cu atoms. Among all the Cu atoms shown in the figure, only five Cu atoms have exclusively Cu neighbors and are neutral in nature; the rest of the Cu are neighbors with at least one Al or O atoms. When a Cu atom is a neighbor with Al or O atoms, bonding or charge transfer occurs. A Cu atom bonded with O atoms is positively charged, whereas a Cu atom bonded with Al atoms is slightly negatively charged and can be understood in terms of difference in electronegativities of Cu and Al. When a Cu atom is bonded with both O and Al atoms, it is charge neutral. The charge compensation is likely to happen in such bonding. The Cu atoms shown in green are therefore almost metallic in nature and are likely to form a conducting channel for the current to flow in the network.

c. Thermally driven conduction fluctuations. In this section, we discuss relatively dramatic thermally induced fluctuations in the HOMO-LUMO splitting and consider the electronic conduction mechanisms.[2] We illustrate with one of the conducting models (including 20% Cu) and performed molecular dynamics (MD) at 1000 K for 24 ps. The fluctuation of the frontier HOMO and LUMO levels with time is provided in Fig. 7. $\eta(t)$ is the HOMO-LUMO splitting through the course of the MD. The model reveals a large thermally driven fluctuation in the value of the HOMO-LUMO gap with time. As we discussed earlier in Sec. III A 2 a, the electronic conductivity is crudely associated with the band gap. Following Eq. (5), for dc conduction to occur, there needs to be finite density of states (N_{ϵ_f}) at the Fermi level (to enable electronic transitions, as from Fermi's golden rule) and nonvanishing matrix elements $|D_{\epsilon_f}|^2$ as in Eq. (1). So, we expect more available states near the Fermi level for the system with small gap, thus, the conductivity $\sigma(t)$ can be very crudely linked to $\eta(t)$ (small $\eta \Rightarrow$ large σ) in the spirit of Landau-Zener tunneling [47,48]. We provisionally interpret the small-gap (small-η) instantaneous configurations as low-resistance states, and the large-gap configurations as high-resistance states.

It is therefore interesting to visualize the conduction-active parts of the network for these different states. We selected two snapshots (shown by orange arrows in Fig. 7), one representing a small gap (low η) and the other large gap (high η) from the simulation and obtained the SPC as described in Sec. II B. The variation of the HOMO-LUMO gap due to

[2]Here and elsewhere in this paper, electronic time evolution refers only to variation in Kohn-Sham eigenvalues/states on the Born-Oppenheimer surface; no attempt is made to solve a time-dependent Kohn-Sham equation.

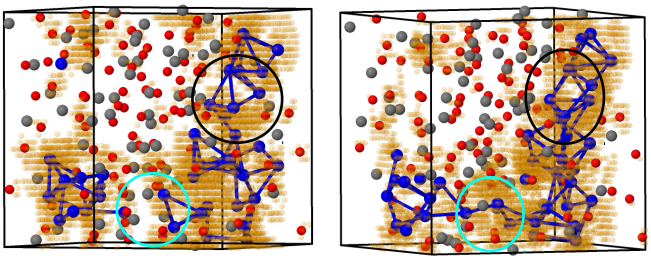

FIG. 8. Overlaying SPC values (orange spheres) with atomic configuration: on the left, large-gap (high-resistance) state of a-Al_2O_3:Cu model with 20% Cu. On the right, small-gap (low-resistance) state of the same system. Color nomenclature: blue, Cu atom; red, O atom; and gray, Al atom. The bond length of cutoff 2.6 Å is chosen. Circles with same color represent the same part of the local configurations. There is a factor of about 10^4 between the conductivity of the two conformations.

thermal fluctuations has also been studied in boron-doped a-Si at 600 K, where it was observed that with addition of hydrogen to the network, there occurs a thermal modulation of HOMO and LUMO states causing the HOMO and LUMO states to be overlapped at a certain interval of the thermal simulation representing highly conducting configuration [49]. This computation makes it clear that the dc conductivity is difficult to accurately estimate since to handle the large electron-phonon coupling for states near the Fermi level, long MD averages at constant temperature would be required (within an adiabatic picture for which one simply averages the Kubo formula over a trajectory).

d. Space-projected conductivity. We investigated SPC by computing $\zeta(x)$ as described in Sec. II B in our models. SPC values are evaluated at coarse three-dimensional (3D) grid points inside the supercells. A graphical representation of SPC values in 3D grid points overlaid with the atomic configuration is shown in Fig. 8. This figure shows the SPC computed on two models: one with large η and the other with and small η. We include 12% of the highest local contributions to SPC in each plot. The SPC reveals that the conduction path is primarily along interconnected Cu atoms. A few O atoms in the vicinity of Cu atoms also participate in the conduction whereas Al atoms do not show any role in the conduction. We see that the SPC for the large-gap snapshot is disconnected so that $\zeta(x)$ appears to be localized in certain region, whereas the SPC with small gap forms an interconnected chain for the conduction. For these two particular structures, we observed the local configurations as shown by the enclosed circles of Fig. 8 where the Cu atoms come closer to form short bonds and form a closed network in the right plot compared to the left plot.

This shows that the connectivity among Cu atoms determines the conductivity of the system. Aside from the structural difference, the type and the number of clusters also affect the HOMO-LUMO gap. It has been shown that an alternation of the HOMO-LUMO gap occurs between even- and odd-numbered isolated clusters due to electron-pairing effects and particularly large gap for cluster size 2, 8, 18, 20, 34, and 40 which are also called as magic clusters [50]. At this temperature, the diffusion of Cu atoms may cause the change in the bonding environment of Cu atoms, resulting in the variation of the gap with time.

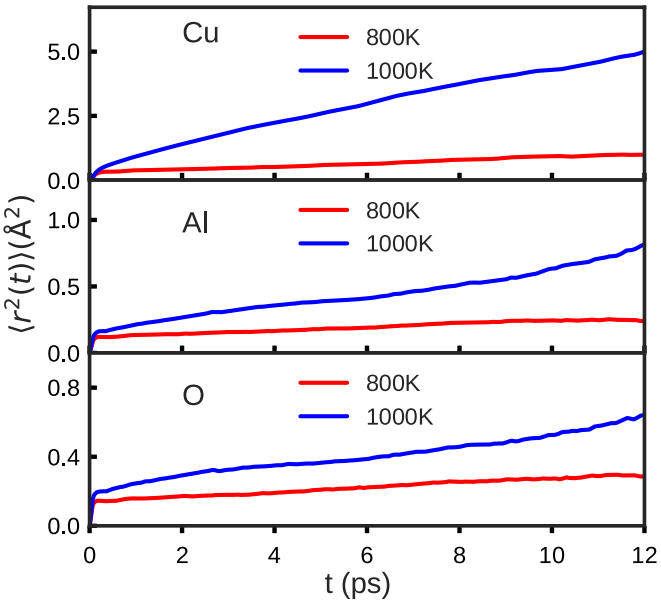

FIG. 9. Mean-squared displacement at 800 and 1000 K for 20% Cu model.

B. Ion and lattice dynamics

Since the ion and lattice dynamics are of key importance for applications, we discuss these in this section.

1. Ionic motion

As a representative example, the 20% model was annealed at different temperatures 800 and 1000 K for 15 ps, and the resulting ion dynamics was studied by calculating the mean-squared displacement for each atomic species as

$$\langle r^2(t)\rangle_\alpha = \frac{1}{N_\alpha}\sum_i^{N_\alpha}\langle|\vec{r}_i(t)-\vec{r}_i(0)|^2\rangle, \tag{6}$$

where N_α represents the number of atoms of species α, $r_i(t)$ represents the position of atom i at time t, and the $\langle\ldots\rangle$ represents an average on the time steps and/or the particles. The connection between mean-squared displacement and the self-diffusion coefficient is given by Einstein's relation

$$\langle r^2(t)\rangle = A + 6Dt, \tag{7}$$

where D is the self-diffusion coefficient, A is a constant, and t is the simulation time. Figure 9 shows the mean-squared displacement for the corresponding species. Clearly, Cu atoms are more diffusive than Al and O atoms. On taking the snapshots of the position of atoms (figures not shown here), we find that the Cu atoms do not diffuse into the host matrix but diffuse within the Cu clusters and thus the Cu clusters become stable at these ranges of temperatures. We then calculated the self-diffusion coefficient for each species using Eq. (7). The diffusion coefficient for Cu at 800 and 1000 K are obtained to be 9.95×10^{-7} cm^2/s and 6.248×10^{-6} cm^2/s, respectively.

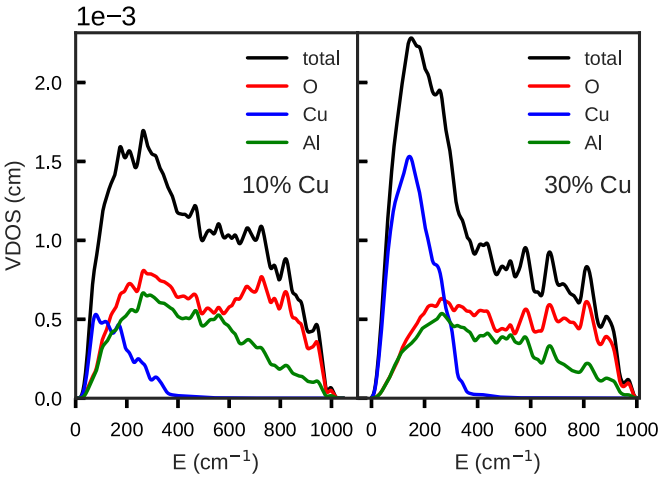

FIG. 10. Normalized total and partial vibrational density of states for 10% and 30% of Cu models.

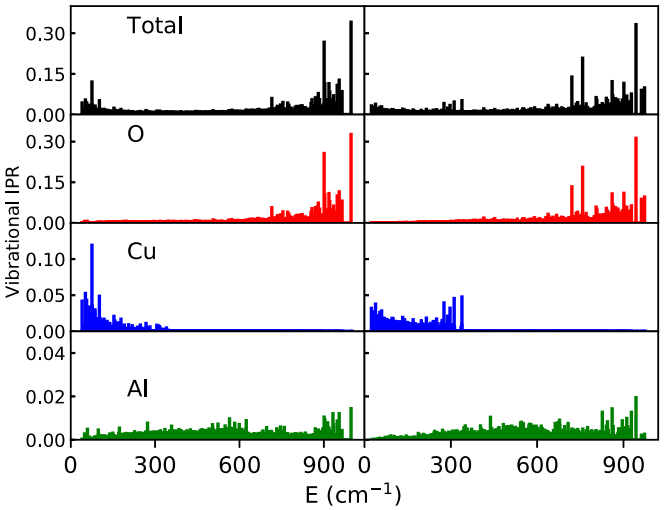

FIG. 11. Vibrational IPR different models. Left column for 10% model and the right column for 30% model.

Cu is relatively static in a-Al_2O_3 compared to chalcogenides [51].

2. Lattice dynamics

We study the lattice dynamics of these Cu-doped systems by the means of vibrational density of states (VDOS), species-projected VDOS, and the vibrational IPR. The properties are studied within the harmonic approximation using the first-principles method. The force constant is obtained by displacing each atom by 0.015 Å along $\pm x$, $\pm y$, and $\pm z$ directions. The diagonalization of the dynamical matrix yields eigenfrequencies and the corresponding eigenmodes. The normalized VDOS and the partial VDOS are expressed as [52]

$$Z(E) = \frac{1}{3N}\sum_n \delta(E - \hbar\omega_n), \tag{8}$$

$$Z_\alpha(E) = \frac{1}{3N}\sum_{i\in\alpha}^{N_\alpha}\sum_n \left|e_i^n\right|^2 \delta(E - \hbar\omega_n), \tag{9}$$

where ω_n are the normalized eigenfrequencies ($3N$ in total). Here, the sum over i is over all the atoms belonging to the species α and e_i^n corresponds to the displacement vector of atom i with Cartesian components $e_{i\mu}^n$ where $\mu = x,\ y$, and z. We approximate the δ function by a Gaussian distribution function of width 10 cm^{-1}. Among the $3N$ eigenmodes, we neglect the first three translational modes with frequency very close to zero.

Figure 10 shows the total and partial VDOS for 10% and 30% Cu content. The lower vibrational modes correspond to the Cu atoms. The higher-frequency modes are unsurprisingly dominated by O atoms. To study the localization of the vibrational eigenstates, we calculated the vibrational IPR for each species. From Fig. 11, we see that the higher modes corresponding to the O atoms are more localized compared to the lower modes for both concentrations of Cu. The lower eigenstates corresponding to Cu for 10% Cu model are quite localized compared to the 30% Cu model. The vibrational states for aluminum are mostly extended for both models.

IV. CONCLUSION

In this paper, we studied realistic models of a-Al_2O_3:Cu, and showed that the Cu atoms have a strong propensity to cluster in the ionic a-Al_2O_3 host. We observed a continuous filling of the optical gap by Cu levels, especially at 20% and 30% models. As the Cu concentration increases (and Cu-Cu connectivity increases), the Cu levels band to enable metallic conduction. We observed the opening and closing of the HOMO-LUMO gap at an elevated temperature, and projected electronic conductivity into real space and visualized the conduction-active parts of the network. We showed that the connectivity of Cu atoms plays a significant role in the electronic conduction. We studied the diffusion of Cu atoms in a-Al_2O_3 at different temperatures and observed that the Cu atoms do not diffuse easily into the a-Al_2O_3 in contrast with relatively covalent chalcogenides like $GeSe_3$ [51]. We discussed the harmonic lattice dynamics of the models by calculating vibrational density of states and the vibrational IPR and showed that the lower vibrational modes correspond to Cu atoms and the higher modes correspond to O atoms.

The results presented in this work on a-Al_2O_3:Cu show an interesting contrast with similar study performed on $GeSe_3$:Ag [53]. We find that the properties of Cu in the oxide host (in this case, a-Al_2O_3) contrast with those of Ag in chalcogenide (in case of [53], $GeSe_3$). The Ag atoms do not form a cluster in the $GeSe_3$ and no uniform filling of the optical gap is observed. In other words, one has to electrochemically work hard to draw Ag atoms together to form a cluster in $GeSe_3$. So, the electronic conduction is likely to occur by hopping process in $GeSe_3$:Ag whereas the conduction in Al_2O_3 is most likely through the interconnected Cu atoms in the network. We observed that Cu in a-Al_2O_3 exhibits different charge states (negative, neutral, and positive) whereas the charge state of Ag in $GeSe_3$ changes from neutral

when isolated to ionic (positive) near the trapping center sites (host atoms) [54].

ACKNOWLEDGMENTS

We thank U. S. NSF support under Grants No. DMR 1507670 and No. DMR 1506836. Some of this work used the Extreme Science and Engineering Discovery Environment (XSEDE), which is supported by National Science Foundation Grant No. ACI-1548562, using BRIDGES at the Pittsburgh Supercomputer Center under the allocation TG-DMR190002. We thank Prof. G. Chen for valuable discussions during this work.

[1] J. G. Simmons and R. R. Verderber, Radio Electron. Eng. **34**, 81 (1967).
[2] R. Waser, R. Dittmann, G. Staikov, and K. Szot, Adv. Mater. **21**, 2632 (2009).
[3] S. Tappertzhofen, I. Valov, T. Tsuruoka, T. Hasegawa, R. Waser, and M. Aono, ACS Nano **7**, 6396 (2013).
[4] M. N. Kozicki and H. J. Barnaby, Semicond. Sci. Technol. **31**, 113001 (2016).
[5] S. Dietrich, M. Angerbauer, M. Ivanov, D. Gogl, H. Hoenigschmid, M. Kund, C. Liaw, M. Markert, R. Symanczyk, L. Altimime, S. Bournat, and G. Mueller, IEEE J. Solid-State Circuits **42**, 839 (2007).
[6] M. Kund, G. Beitel, C. Pinnow, T. Rohr, J. Schumann, R. Symanczyk, K. Ufert, and G. Muller, *IEEE InternationalElectron Devices Meeting, 2005, IEDM Technical Digest* (IEEE, Piscataway, NJ, 2005), pp. 754–757.
[7] D. Lee, S. Oukassi, G. Molas, C. Carabasse, R. Salot, and L. Perniola, IEEE J. Electron Devices Soc. **5**, 283 (2017).
[8] W. Chen, S. Tappertzhofen, H. J. Barnaby, and M. N. Kozicki, J. Electroceram. **39**, 109 (2017).
[9] T. Tsuruoka, K. Terabe, T. Hasegawa, and M. Aono, Nanotechnology **21**, 425205 (2010).
[10] T. Gu, T. Tada, and S. Watanabe, ACS Nano **4**, 6477 (2010).
[11] X. Xu, J. Liu, and M. P. Anantram, J. Appl. Phys. **116**, 163701 (2014).
[12] A. Belmonte, W. Kim, B. Chan, N. Heylen, A. Fantini, M. Houssa, M. Jurczak, and L. Goux, *2013 5th IEEE International Memory Workshop* (IEEE, Piscataway, NJ, 2013), pp. 26–29.
[13] A. Belmonte, U. Celano, R. Degraeve, A. Fantini, A. Redolfi, W. Vandervorst, M. Houssa, M. Jurczak, and L. Goux, IEEE Electron Device Lett. **36**, 775 (2015).
[14] S. C. Pandey, R. Meade, and G. S. Sandhu, J. Appl. Phys. **117**, 054504 (2015).
[15] T. Tsai, F. Jiang, C. Ho, C. Lin, and T. Tseng, IEEE Electron Device Lett. **37**, 1284 (2016).
[16] M. Barci, G. Molas, C. Cagli, E. Vianello, M. Bernard, A. Roule, A. Toffoli, J. Cluzel, B. D. Salvo, and L. Perniola, IEEE J. Electron Devices Soc. **4**, 314 (2016).
[17] J. Kittl, K. Opsomer, M. Popovici, N. Menou, B. Kaczer, X. Wang, C. Adelmann, M. Pawlak, K. Tomida, A. Rothschild *et al.*, Microelectron. Eng. **86**, 1789 (2009).
[18] P. Eklund, M. Sridharan, G. Singh, and J. Bøttiger, Plasma Proc. Polym. **6**, S907 (2009).
[19] K. Prasai, K. N. Subedi, K. Ferris, P. Biswas, and D. A. Drabold, Phys. Status Solidi: Rapid Res. Lett. **12**, 1800238 (2018).
[20] G. Gutiérrez, A. B. Belonoshko, R. Ahuja, and B. Johansson, Phys. Rev. E **61**, 2723 (2000).
[21] P. Vashishta, R. K. Kalia, A. Nakano, and J. P. Rino, J. Appl. Phys. **103**, 083504 (2008).
[22] A. Miranda Hernández J. G., Soto Guzmán and E. Rocha-Rangel, J. Ceram. Proc. Res. **7**, 311 (2006).
[23] G. Kresse and J. Hafner, Phys. Rev. B **47**, 558 (1993).
[24] P. E. Blöchl, Phys. Rev. B **50**, 17953 (1994).
[25] G. Kresse and D. Joubert, Phys. Rev. B **59**, 1758 (1999).
[26] J. P. Perdew and A. Zunger, Phys. Rev. B **23**, 5048 (1981).
[27] D. A. Drabold, Eur. Phys. J. B **68**, 1 (2009).
[28] H. Momida, T. Hamada, Y. Takagi, T. Yamamoto, T. Uda, and T. Ohno, Phys. Rev. B **73**, 054108 (2006).
[29] R. Kubo, J. Phys. Soc. Jpn. **12**, 570 (1957).
[30] D. A. Greenwood, Proc. Phys. Soc. **71**, 585 (1958).
[31] R. M. Feenstra and M. Widom, www.andrew.cmu.edu/user/feenstra/wavetrans.
[32] E. N. Economou and C. M. Soukoulis, Phys. Rev. Lett. **46**, 618 (1981).
[33] H. U. Baranger and A. D. Stone, Phys. Rev. B **40**, 8169 (1989).
[34] R. B. S. Oakeshott and A. MacKinnon, J. Phys.: Condens. Matter **6**, 1513 (1994).
[35] M. Paulsson and M. Brandbyge, Phys. Rev. B **76**, 115117 (2007).
[36] P. Lamparter and R. Kniep, Phys. B (Amsterdam) **234-236**, 405 (1997).
[37] C. Landron, L. Hennet, T. E. Jenkins, G. N. Greaves, J. P. Coutures, and A. K. Soper, Phys. Rev. Lett. **86**, 4839 (2001).
[38] E. A. Chagarov and A. C. Kummel, J. Chem. Phys. **130**, 124717 (2009).
[39] S. K. Lee *et al.*, Phys. Rev. Lett. **103**, 095501 (2009).
[40] K. Sankaran, L. Goux, S. Clima, M. Mees, J. Kittl, M. Jurczak, L. Altimime, G.-M. Rignanese, and G. Pourtois, ECS Transactions **45**, 317 (2012).
[41] J. A. Dawson and J. Robertson, J. Phys. Chem. C **120**, 14474 (2016).
[42] J. M. Ziman, *Models of Disorder: The Theoretical Physics of Homogeneously Disordered Systems* (Cambridge University Press, Cambridge, England, 1979), pp. xiii, 525.
[43] N. F. Mott and E. A. Davis, in *Electronic Processes in Non-crystalline Materials*, 2nd ed., edited by N. F. Mott and E. A. Davis (Clarendon, Oxford, 1979), pp. xiv, 590.
[44] K. Prasai, G. Chen, and D. A. Drabold, Phys. Rev. Mater. **1**, 015603 (2017).
[45] D. M. Guzman and A. Strachan, Phys. Rev. Mater. **1**, 055801 (2017).
[46] W. Tang, E. Sanville, and G. Henkelman, J. Phys.: Condens. Matter **21**, 084204 (2009).

[47] L. Landau, Phys. Z. Sowjetunion **2**, 46 (1932).
[48] C. Zener, Proc. R. Soc. London A **137**, 696 (1932).
[49] A. Pandey, B. Cai, N. Podraza, and D. A. Drabold, Phys. Rev. Appl. **2**, 054005 (2014).
[50] M. Kabir, A. Mookerjee, and A. K. Bhattacharya, Phys. Rev. A **69**, 043203 (2004).
[51] B. Prasai and D. A. Drabold, Phys. Rev. B **83**, 094202 (2011).
[52] A. Pasquarello, J. Sarnthein, and R. Car, Phys. Rev. B **57**, 14133 (1998).
[53] K. N. Subedi, K. Prasai, and D. A. Drabold, arXiv:1901.04324.
[54] I. Chaudhuri, F. Inam, and D. A. Drabold, Phys. Rev. B **79**, 100201(R) (2009).